Experimental and theoretical study of defect-driven scintillation from $\gamma-Ga_2O_3$ nanophosphor-embedded transparent glass-ceramics

Chunli Fan,[1] Wenhao Li,[1] Jinlong Nan,[1] Peng Hu,[3] Sen Qian,[3] Yao Zhu,[1] Yan Sun,[1] Qingmiao Hu,[4] Zhehao Hua,[3] Ci Wang,[1,2,*] Jing Ren,[1,2,†] and Jianzhong Zhang[1,2]

[1]*College of Physics and Optoelectronic Engineering, Harbin Engineering University, Harbin 150001, China*
[2]*National Key Laboratory of Underwater Acoustic Technology, Harbin Engineering University, Harbin 150001, China*
[3]*Institute of High Energy Physics, Chinese Academy of Sciences, Beijing 100049, China*
[4]*Institute of Metal Research, Chinese Academy of Sciences, 72 Wenhua Road, Shenyang 110016, China*

(Received 11 July 2023; accepted 27 September 2023; published 11 October 2023)

Gallium oxide (Ga_2O_3), as a representative of the four-generation ultrawide band-gap semiconductors, emerges to be a promising candidate for high performance scintillators. However, the full exploitation of its scintillation properties and the understanding of the defect-driven luminescence mechanisms are still lacking especially for $\gamma-Ga_2O_3$ nanocrystals (NCs) grown in glass. Here, the easy-to-process glass-making and post-thermal treatment method is used to prepare $\gamma-Ga_2O_3$ NC embedded transparent glass-ceramics (GCs). X-ray excited bright visible blue-green emissions are observed from the $\gamma-Ga_2O_3$ NC embedded GCs, which are attributed to the donor-acceptor pair (DAP) recombination. Positive luminescence hysteresis is found to occur in the processes of both ultraviolet (UV) light excited photoluminescence and the x-ray excited luminescence (XEL). A method of prolonged UV preirradiation is used to counteract the hysteresis effect, which is desirable from the application point of view. Monte Carlo simulation is employed to reveal the difference between x- and $\gamma-$ray photoresponse of the GCs, and the results are compared with those of the $Bi_4Ge_3O_{12}$ crystal. First-principles calculations are carried out to investigate the intrinsic defect properties of $\gamma-Ga_2O_3$. Our results provide a theoretical foundation to understand the relevant defects responsible for the observed DAP, and offer potential avenues for tailoring optical performance for various applications. As a proof-of-concept, an x-ray imaging system is built on the studied GC scintillator, exhibiting performance superior to that of the eye-catching $CsPbBr_3$ perovskite NC embedded GCs.

DOI: 10.1103/PhysRevB.108.155414

I. INTRODUCTION

The increasing demand in ionizing radiation detection for medical diagnostics, homeland security, environmental monitoring, high-energy physics, and resource exploration, etc., has highlighted the importance of developing robust and cost-efficient scintillators [1–4]. Recently, transparent (ultra)wide-band-gap third- and next-generation semiconductor single crystals, such as ZnO and Ga_2O_3, etc., have attracted much attention for their high excitation energy conversion efficiency due to high mobility of free charge carriers, which translates into efficient and fast scintillation in the ultraviolet (UV)-visible wavelength region [5–12]. Unlike rare-earth (RE: Ce^{3+}, Pr^{3+}) dopant activated counterparts, semiconductor scintillators produce emissions by the host material *per se* (known as self-activated scintillators), being subject to the preparation methodology, the presence of defects (either native or extrinsic), and impurities (either unintentional or intentional) [13]. For example, the doping of Ga in ZnO has demonstrated its potential as an ultrafast scintillator due to free exciton radiative recombination producing a light yield (LY) of 5000 ph/MeV [14]. However, ZnO:Ga displays a relatively weak $\gamma-$ray stopping power and suffers from severe thermal quenching of scintillation at room temperature (RT) [9]. In comparison, Ga_2O_3 with a larger band gap ranging 4.6–5.3 eV (related to different polymorphs with different structure symmetries) and a higher density of 5.96 – 6.4 g/cm^3 (versus 5.6 g/cm^3 of ZnO) stands out for its superior attributes such as being more robust with a higher breakdown electric field (8 MV/cm), and having a greater attenuation coefficient as well as a larger LY (>10 000 ph/MeV) [15]. This makes Ga_2O_3 of great interest in areas such as sun-blind detectors and high-energy ray detection. Guo *et al.*'s research shows that Ga_2O_3-based blind detectors have high sensitivity and a low false alarm rate, and Zn, Sn, and Mg plasma is conducive to the enhancement of detector performance [12,16–19]. And in the field of radiation detection, in fact, among the semiconductor scintillators developed so far, Ga_2O_3 has been confirmed to hold the record of LY.

As known today, there exist five commonly identified polymorphs of Ga_2O_3, denoted by α, β, γ, δ, ε. Among them, monolithic $\beta-Ga_2O_3$ is the most thermodynamically stable one at RT. In 2016, Yanagida *et al.* attested to the feasibility of using bulk $\beta-Ga_2O_3$ for $\gamma-$ray detection. A clear full-energy peak was resolved in the pulse height spectrum of ^{137}Cs γ rays, based on which the LY was estimated to be

*Corresponding author: 2520210429@hrbeu.edu.cn
†Corresponding author: ren.jing@hrbeu.edu.cn

15 000 ph/MeV at RT (comparable to that of the commercial Ce^{3+}: YAP crystal, ∼ 12000 ph/MeV). The scintillation decayed with a fast component of only 8 ns and a slow one of 977 ns. Overall, the performance is superior to that of Te-doped ZnSe and comparable to that of Te-doped CdS scintillators [20]. Mykhaylyk *et al.* further explored the performance of $\beta-Ga_2O_3$ as a cryogenic scintillator. The LY was found to increase with decrease in temperature, reaching a maximum value of 19 300 ph/MeV at 50 K. A highly sensitive x-ray detector (338.9 $\mu C\,Gy^{-1}\,cm^{-2}$) was constructed on $\beta-Ga_2O_3$:Mg [21]. The doping of Mg^{2+} greatly improves the sensitivity and speeds up the photoresponse of $\beta-Ga_2O_3$ through modulation of defect concentration.

So far, the scintillation performance of the other polymorphs rather than $\beta-Ga_2O_3$ has been largely left unexplored, despite the encouraging fact that $\gamma-Ga_2O_3$ has exhibited superior photoluminescence (PL) properties [22,23]. However, because of the synthetic barrier, the preparation of $\gamma-Ga_2O_3$ has been mostly limited to nanocrystals (NCs) [24–27]. Radovanovic *et al.* demonstrated that colloidal $\gamma-Ga_2O_3$ NCs exhibit size-tunable PL in the visible blue-green region. The fact that $\gamma-Ga_2O_3$ is capable of energy harvesting of deep UV photons (specifically in the UV-C spectrum of 200–280 nm) has pointed to its potential of being used for solar-blind photodetection [28]. Through a post-thermal treatment of a specially designed glass featured by unique amorphous phase separation, Sigaev *et al.* managed to grow $\gamma-Ga_2O_3$ NCs inside (and thus being hosted by) the glass matrix, and proved that the inherent size-dependent PL properties of $\gamma-Ga_2O_3$ NCs were maintained [29]. Promising results have been obtained as to the use of $\gamma-Ga_2O_3$ NCs embedded glasses (a.k.a., glass-ceramics, GCs) for a variety of enabling applications including: UV-to-visible light conversion, photocatalysis, and near-infrared (NIR) light sources when doped with transition metal ions (e.g., Cr^{3+}, Ni^{2+}) [29–32]. Intentionally growing optical functional NCs in robust, chemically inert, and easy-to-process glasses, demonstrated by the authors of the present paper and by many other researchers, represents an ideal testbed for acquiring unprecedented qualities of GCs, because they integrate favorably both the advantages of crystals and glasses, such as the high radiative emission efficiency of crystals, and the waveguiding capability of glasses [33–35].

Previous research has demonstrated that $\gamma-Ga_2O_3$ exhibits a defective cubic spinel structure (space group $Fd\bar{3}m$), similar to that of $\gamma-Al_2O_3$, which plays an essential role in determining luminescence properties [36]. Studies have revealed the presence of vacancies at both cation and anion sites in the $\gamma-Ga_2O_3$ lattice [37,38]. The observed blue-green emission is generally attributed to the recombination of electrons trapped by oxygen vacancies and holes by gallium vacancies and Ga-O divacancies, known as the donor-acceptor pair (DAP) recombination [39]. However, there remains a very limited understanding of the scintillation properties of $\gamma-Ga_2O_3$ NCs (specifically when they are grown in glass). In addition, the theoretical calculation of the electronic structure and defect states of $\gamma-Ga_2O_3$ have yet to be reported, representing an exciting avenue for physics exploration and materials optimization.

In this work, we synthesized transparent GCs containing $\gamma-Ga_2O_3$ NCs via the simple thermal treatment (i.e., controlled crystallization of a precursor glass) [Fig. 1(a)]. The scintillation properties of such GC scintillators were investigated regarding x-ray excited luminescence (XEL), scintillation decay time, and thermal stability. Positive luminescence hysteresis (also known as bright burn or sensitization, increase in emission intensity following previous irradiation) was found to occur both in the PL and XEL emissions. Monte Carlo simulation was employed to reveal the difference in energy deposition capacity of the GCs for x and γ rays. The first-principles calculations were used to appreciate the intrinsic defects responsible for the scintillation of $\gamma-Ga_2O_3$. The theoretical analysis of defects and their impact on the optical properties of $\gamma-Ga_2O_3$ provides valuable insight into the underlying mechanisms governing its luminescence behavior. An x-ray imaging system was built on the studied GC scintillators with reasonably good performance.

II. EXPERIMENTAL AND COMPUTATIONAL DETAILS

A. Preparation of $\gamma-Ga_2O_3$ NCs embedded GCs

Samples with the nominal composition of $25SiO_2-45GeO_2-20Ga_2O_3-2.5Na_2O-7.5Li_2O$ (in mol. %) were prepared by the melt quenching method. The raw materials were used of high purity (4N, Aladdin Corp) SiO_2, GeO_2, Ga_2O_3, Na_2CO_3, and Li_2O compounds. The mixed raw materials were melted at 1500° C in a quartz crucible in air for 40 min. The melt was quenched onto a copper mold preheated at 250° C and quickly transferred to a muffle furnace for annealing at 550° C for 3 h, forming precursor glasses (PGs). The PGs were cut into appropriate sizes, heat treated at 680° C for 5, 8, and 10 h, respectively, obtaining GCs that are denoted by SGL5, SGL8, and SGL10, respectively. Finally, the GCs were polished to the desired morphology and surface finish.

B. Characterization of microstructure, PL, transmission, scintillation and x-ray imaging properties

The crystal phase of samples was determined using an x-ray diffractometer (XRD) (D/MAX 2550VB/PC, Rigaku Corporation, Japan). The microstructure of samples was studied using transmission electron microscopy (TEM) (FEI Talos F200x, American FEI Company). Steady-state and time-resolved PL spectra, PL excitation (PLE), and PL quantum yield (PLQY) were measured as one can refer to in our previous work [40]. Transmission spectra were measured by a spectrophotometer (Perkin-Elmer Lambda-950). X-ray excited luminescence (XEL) spectra were measured in the reflection mode by a Zolix Omni-A 300i spectrometer equipped with an x-ray tube (MOXTEK Tube-MAN-1006, Cu target, 50 kV) and a homemade temperature controller. The scintillation decay time was measured using the delayed coincidence single photon counting method, and the samples were excited by a ^{137}Cs $\gamma-$ray source. The time profiles were registered using two Hamamatsu PMTs (R1104, R928), a Canberra TAC/SCA 2145 time-to-amplitude converter, and a Tukan-8K-USB MCA.

The x-ray imaging system consisted of an x-ray source, a scintillator, and a complementary metal-oxide-semiconductor

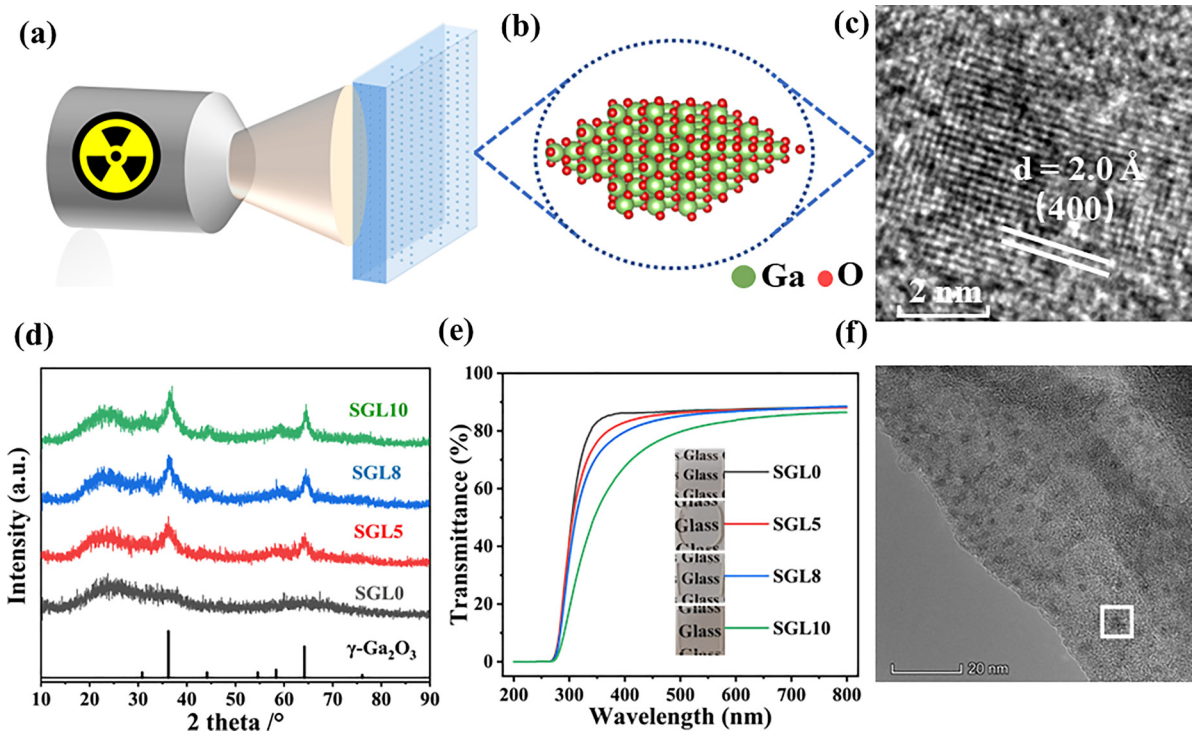

FIG. 1. (a) Schematic of x-ray detection using the $\gamma-Ga_2O_3$ NC embedded transparent GC. (b) Demonstration of the crystal structure of $\gamma-Ga_2O_3$. (c) High resolution TEM images of a single $\gamma-Ga_2O_3$ NC. (d) XRD patterns and (e) transmission spectra of the SGL0, SGL5, SGL8, and SGL10 samples. Inset: digital photos of the samples under the natural light. (f) TEM images of the SGL5 sample.

camera (QHY163M). The x-ray source was a Magpro 12-W x-ray tube with a tungsten (W) target, operating at the voltage of 60 kV. The tube current was adjusted within the range 100–200 μA to control the x-ray dose rate. The object (used for imaging) and scintillator were positioned perpendicular to the incident x rays, with the scintillator sited behind the object.

C. Monte Carlo simulation

Monte Carlo simulations using the GEANT4 (Geometry and Tracking 4) package [41] were conducted to simulate the energy deposition in samples with the dimension of 10 mm×10 mm×2 mm. The γ ray source was a ^{137}Cs source, positioned 2 mm away from the scintillator center and incident in a cone shape with an incident angle of 160°. In the simulations, the energy resolution was set to 5% and the energy threshold was defined as 50 KeV for x rays and 662 KeV for γ rays. The radiation-matter interactions were treated as electromagnetism interactions, as specified in the Physics Reference Manual of GEANT4 [34].

D. Density function theory calculation

The projector augmented wave (PAW) method [42] was used to determine the structure of $\gamma-Ga_2O_3$ via Vienna Ab initio Simulation (VASP) code [43,44], which is based on the density function theory (DFT). Energy cutoff was set as 520 eV to truncate the plane waves basis functions. The Perdew-Burke-Ernzerhof (PBE, for structure relaxations) functional [45] and Heyd-Scuseria-Ernzerhof (HSE, for electron structure calculations) functional [46,47] under generalized gradient approximation (GGA) were used for exchange and correlation terms [48]. Ga $3d^{10}4s^24p^1$ and O $2s^22p^4$ were treated as the valence state. A K-point mesh of 8×8×4 based on the Monkhorst-Pack scheme was used to sample the Brillouin zone [49]. The structural optimization process was considered converged when the Hellmann-Feynman forces on all atoms were below 5×10^{-2} eV/Å. The self-consistent field (SCF) method was used for both structural optimization and electronic structure calculations, with a convergence criterion of 10^{-4} eV. To simulate a reasonable structure, a 40-atom supercell was created by expanding the primitive cell of the spinel structure three times along the c axis, as described in the literature [50]. Within this supercell, two cationic sites were chosen to be vacant, resulting in a vacancy-vacancy distance of 8.06 Å. The calculation was given of the available equilibrium chemical potential region for $\gamma-Ga_2O_3$ in the two-dimensional (μ_{Ga}, μ_O) plane (see Fig. S1 of the Supplemental Material [51]) to verify the validity of the following calculations of electronic structures [52,53].

III. RESULTS AND DISCUSSION

A. Microscopy analyses, transmission, and PL properties

Figure 1(c) illustrates the XRD patterns of samples. Sharp crystal diffraction peaks are clearly observed in all the patterns of GCs (SGL5, SGL8, and SGL10), which match well with those of $\gamma-Ga_2O_3$ (JCPDS No. 20–0426). The diffraction peaks of GCs become sharper as thermal treatment time increases, indicative of growing size of NCs in glass. In contrast, the structureless XRD pattern of PGs (SGL0) is characteristic of amorphous glass. A close examination of its XRD pattern

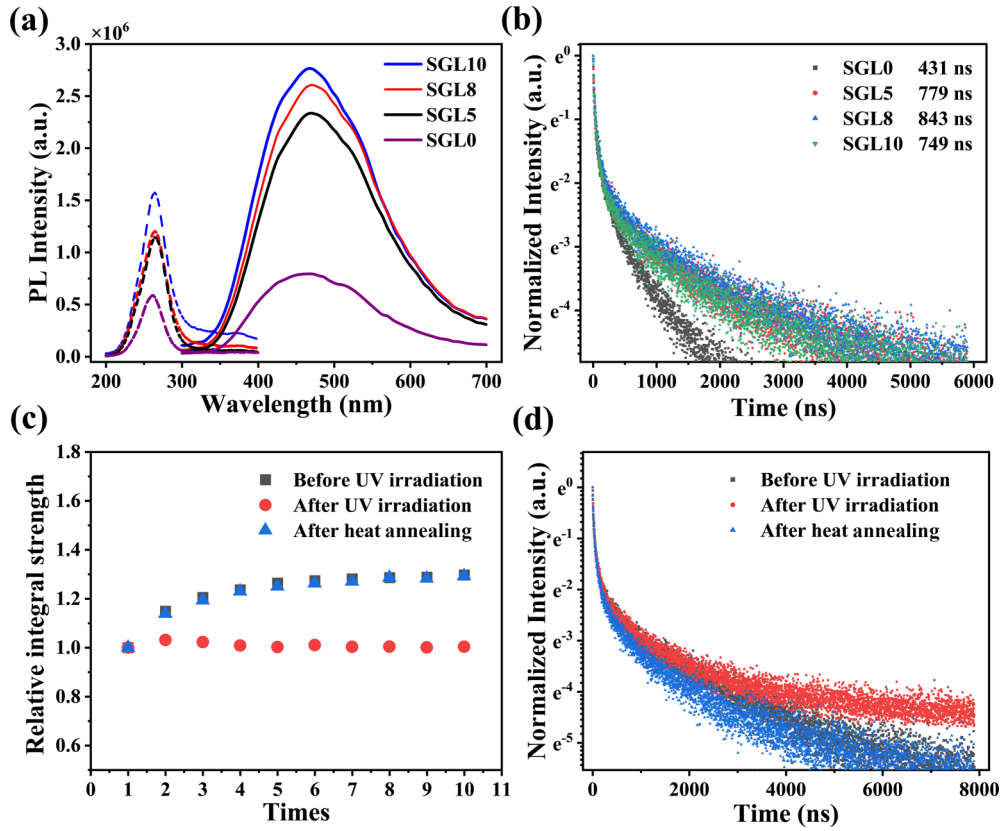

FIG. 2. (a) PL emission spectra of the samples excited by a 264-nm xenon lamp and the corresponding excitation spectra monitored at the 470-nm emission. (b) Normalized PL decay curves of the samples by monitoring the 470-nm emission. (c) Variations of integrated PL intensity of SGL5 under repeated UV excitations, before and after an UV preirradiation (at 264 nm for 60 min), and after a further thermal reannealing (at 300 °C for 60 min). (d) Normalized PL decay curves of SGL5 before and after the UV preirradiation, and after the further thermal treatment.

also shows a weak shoulder band at around $2\theta = 36^\circ$, which is coincident with the diffraction peak of $\gamma-Ga_2O_3$ and suggests the occurrence of submicrometer amorphous phase separation [32]. Figure 1(f) shows the microscopic morphology of SGL5, where NCs with an average size of 5 nm are uniformly dispersed in the glass matrix. It is necessary to keep the particle size of NCs as small as possible, because the large refractive indices difference between Ga_2O_3 (>1.9) and the glass matrix (∼ 1.6) tends to induce significant scattering losses. The transmission of the GCs decreases with increase in thermal treatment time especially around the cutoff wavelength as shown in Fig. 1(e). This can be accounted for by the increase in the particle size of $\gamma-Ga_2O_3$ NCs as confirmed by the XRD data.

Both the PG and GC samples exhibit a broad PL emission band ranging from the UV to visible blue-green region and peaking around 470 nm, when excited by a xenon lamp emitting at 264 nm, as depicted in Fig. 2(a). The PL emission and excitation spectra (when examined at the peak 470-nm emission) of the samples show minimal overlap, indicating a large Stokes shift and a negligible self-absorption. It is interesting to note that the PLE spectra are limited to the whole UV-C region (200–280 nm), pointing to the potential of uses in solar-blind detection [29]. The PLQYs of the samples were determined to be 4.48%, 7.69%, 8.21%, and 7.56%, for SGL0, SGL5, SGL8, and SGL10, respectively. The PLQYs are less than in the case of chemically synthesized colloidal $\gamma-Ga_2O_3$ NCs (30%) [54], possibly due to resulting quenching from interfaces between $\gamma-Ga_2O_3$ NCs and the glass matrix. With the increase in heat treatment time, the PL emission intensity and quantum efficiency are improved. The normalized PL decay curves are depicted in Fig. 2(b), which can be fitted by a third-order exponential function [55,56]. The fitting formula is as follows:

$$y = \sum_{i=1} A_i e^{-x/\tau_i} + y_0 \quad (i = 1, 2, 3 \ldots),$$

$$\tau_{\text{average}} = \frac{\sum_{i=1} A_i \tau_i^2}{\sum_{i=1} A_i \tau_i},$$

where y_0 is the baseline position, A_i represents the amplitude of the pulse, t_i is the decay time, and τ_{average} is the average decay time. The fluorescence attenuation life of glass-ceramics is shown in Table I. The calculated average lifetimes are 431, 779, 843, and 745 ns, respectively, for SGL0, SGL5, SGL8, and SGL10. The decay time appears to increase with thermal treatment time.

The blue-green emissions have been proposed to originate from the tunnel recombination of an electron on a donor (composed of an oxygen vacancy $[V_O]^X$) with a hole on an acceptor (which could be either a triply charged gallium vacancy $[V_{Ga}]'''$ or a pair of singly charged divacancies $[V_O, V_{Ga}]'''$),

TABLE I. The fluorescence attenuation lifetime values of different glass samples were fitted with third-order exponents, and the average lifetime was calculated.

Name	A_1	τ_1 (ns)	A_2	τ_2 (ns)	A_3	τ_3 (ns)	$\tau_{average}$
SGL0	0.61	10.23	0.28	80.24	0.11	582.70	430.85
SGL5	0.50	11.46	0.38	80.75	0.12	1005.31	779.11
SGL8	0.57	16.10	0.33	93.91	0.10	1113.65	842.87
SGL10	0.55	10.83	0.35	79.44	0.10	992.41	748.84

viz., through the so-called donor-acceptor pair recombination [57]. That the emissions are broad and exhibit large Stokes shifts is indicative of a strong electron-phonon coupling, and suggests the localized nature of the recombining electrons and holes. As will be discussed later by the first principles calculation, both kinds of acceptors may contribute to the observed emissions, albeit Binet *et al.* suggested that the presence of the singly charged divacancy is more likely than the heavily charged gallium vacancy [58]. A previous study of size-dependent PL decay dynamics has indicated that the recombination rate is inversely proportional to the size of $\gamma-Ga_2O_3$ NCs (reflecting the separation distance between donor and acceptor sites) [39]. Following this line, the lengthening of decay time with thermal treatment time is correlated with the growth of the NCs (cf. XRD data).

Positive hysteresis was observed in the $\gamma-Ga_2O_3$ embedded GCs. Specifically, the integral PL intensity gradually increases with accumulated 264-nm UV excitations until a saturation (130% of the original value) is reached as shown in Fig. 2(c). However, the presence of $\gamma-Ga_2O_3$ crystals was not detected in the samples without superheat treatment, for example, there was no corresponding diffraction peak in XRD, so no obvious positive luminescence hysteresis was observed in SGL0 sample (see Fig. S2 of the Supplemental Material [51]). During the irradiation, excited free electrons may progressively fill in shallow defect-related levels. As those defects working as traps compete with radiative recombination centers in capturing the free electrons, the population of the defects tend to increase the probability for free carriers to end up on the recombination centers [4]. Similar effects were also observed in Tb^{3+} or Yb^{3+} doped glasses, and accounted for by filling defect-related traps [59,60]. It is interesting to note that the hysteresis effect greatly attenuates after a prolonged UV preirradiation (at 264 nm for 60 min). That is, the PL intensity barely changes during the second round of PL measurements under repeated UV excitations. Our results well demonstrate the important role that sufficient filling of all stable competing traps plays in reducing the hysteresis effect, which is desirable for reliable UV-to-visible conversion and dosimetry applications (e.g., solar-blind detection, etc.).

We also verified that the hysteresis recovers following a further thermal annealing at 300 °C for 60 min, because heating facilitates the release of trapped electrons (via a temperature dependent detrapping process) [60]. To gain more insight on the defect-driven emissions, the PL decay dynamics was compared before and after the UV preirradiation, and after the further thermal treatment, as shown in Fig. 2(d). The PL decay curves largely overlap in the fast decay portion (<100 ns) in all cases. However, the higher background of the decay curve in the slow decay portion (>100 ns) after the preirradiation indicates a stronger degree of afterglow, possibly due to the "energy storage or memory effect" via the intrinsic defects. Similar results were also found in the case of x-ray preirradiation (results are not shown here).

B. Experimental and theoretical study of scintillation properties

Upon x-ray excitation, the PG sample SGL0 is only weakly emitting, whereas the $\gamma-Ga_2O_3$ embedded GC samples SGL5, SGL8, and SGL10 display strong XEL emissions in the visible-blue-green region similar to PL emissions [Fig. 3(a)]. The XEL intensity increases with longer duration of heat treatment. The XEL emissions also originate from the defect-driven donor-acceptor pair recombination as discussed above. The greatest integral XEL intensity of the GCs is approximately 50% of BGO under the same experimental condition. Figure 3(b) illustrates the integral XEL intensity of the SGL5 as a function of radiation dose rate. A good linear relationship is achieved with the goodness of fitting 99.9%. The results suggest the potential application of $\gamma-Ga_2O_3$ embedded GCs for x-ray detection.

Positive luminescence hysteresis was also observed in XEL [Fig. 3(c)]. Such effect is not a common phenomenon and is reported in a few crystals, including CsI:Tl, $Bi_4Ge_3O_{12}$ (BGO), $Lu_2Si_2O_7$:Pr (LPS:Pr), $Lu_3Al_5O_{12}$:Ce (LuAG:Ge), and $Lu_{0.3}Y_{0.7}AlO_3$:Ce (LuYAP:Ce) [4,61]. The highest integral XEL intensity is 1.15 times the initial value because of the hysteresis effect. However, starting from the fifth time of repeated excitations, the XEL intensity begin to fall with accumulated x-ray dosage until saturation is approached. This contrasts with the results shown in Fig. 2(c) where a plateau was achieved in PL emissions during repeated UV excitations. The discrepancy likely owns its origin to newly created defects by high energy x rays that compete with luminescence centers in trapping free carriers. The formation of defects is indirectly reflected by the appearance of dark spots on samples (viz., photodarkening vivid to the eyes) after repeated x-ray irradiations. The hysteresis effect was retested after subjecting the sample to the UV preirradiation. In Fig. 2(c), we have just proved that the UV preirradiation works efficiently to fill in the intrinsic defects of GCs, and thus suppresses the hysteresis effect. Here, it is noted that the XEL intensity monotonically decreases after the UV preirradiation [Fig. 3(c)], resulting from the dominating role of x rays in creating luminescence quenching centers (defects). Thermal annealing almost completely restores the exposed samples to their original configuration, viz., the same hysteresis reappears with slight difference possibly arising from inefficiency in emptying deep traps at the set temperature. The existence of hysteresis may cause ghosting in imaging, which is one of the problems to be solved in scintillation. If this effect can be controlled reasonably, it may be able to control the enhancement of scintillation LYs. Since such effect closely relates to defects present in the GCs, our future work will explore the strategy of codoping with suitable ions that intentionally create deep traps with the right concentration for quality improvement [61].

The thermal stability of GCs was examined during a heating-cooling cycle from RT to 300° C and back to RT

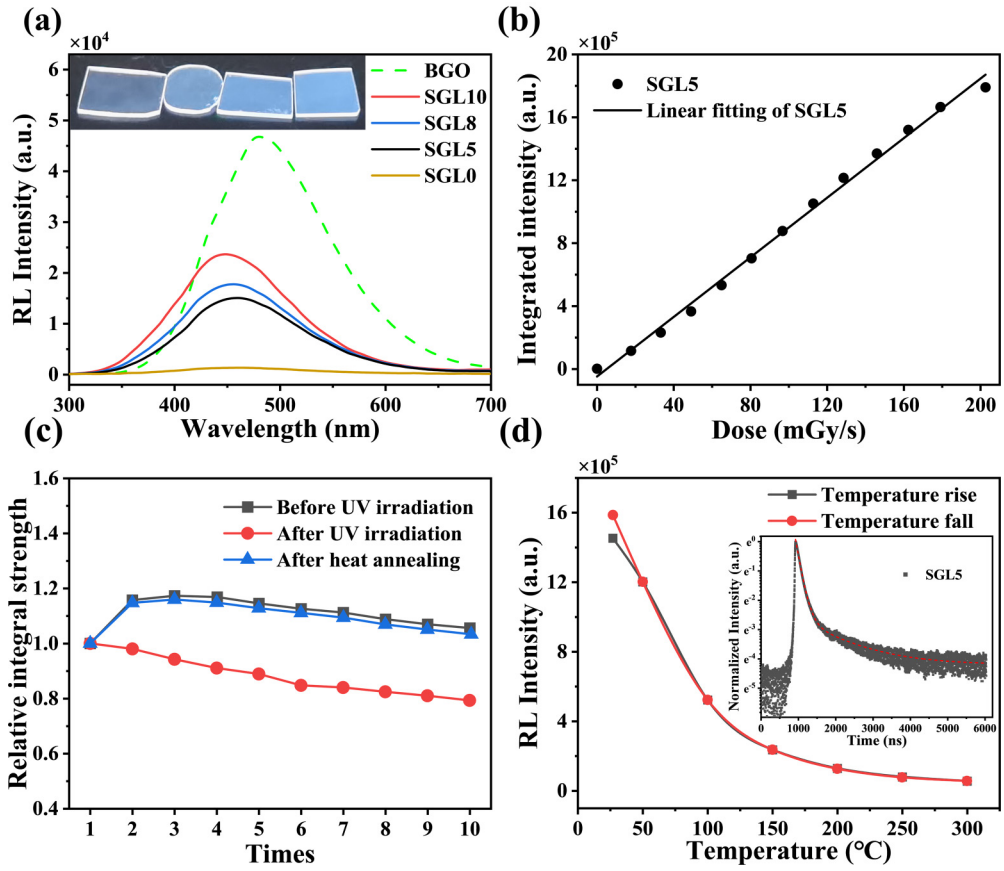

FIG. 3. (a) X-ray excited luminescence (XEL) spectra of the samples and the BGO crystal measured under the same experimental conditions. Inset: digital photos of the samples under x-ray irradiation. (b) Variation of the integral XEL intensity of the samples as a function of irradiation dose rate. The data are well fitted linearly (solid line). (c) Variation of the integral XEL intensity under repeated measurements. Each test comprises an irradiation dose rate of 202.8 $mGy_{air/s}$ for 5 min. The lines are drawn to guide the eyes. (d) Variations of the XEL intensity during a heating-cooling cycle. Inset: Scintillating decay curve of SGL5 under the ^{137}Cs $\gamma-$ray excitation. The curve is fitted by a double-exponential function (dotted line).

as shown in Fig. 3(d). As temperature increases, the XEL intensity gradually decreases, and nearly vanishes at 300° C. During the cooling, the XEL intensity returns to its initial values. The slight difference in the XEL intensities at RT is caused by the presence of the positive hysteresis. The scintillation decay lifetime of the GC sample SGL5 under the ^{137}Cs $\gamma-$ray excitation was evaluated [inset in Fig. 3(d)], which consists of a fast decay (127.46 ns, 74%) and slow (1093.53 ns, 26%) components. As the scintillation process involves energy conversion, transfer, and radiative recombination [Fig. 6(d), see below], the scintillation decay is characterized by a slow decay component. The fact that we failed to record the 632-keV γ-ray photoabsorption peak from the pulsed height spectrum measurement prohibits the evaluation of the LYs of the studied samples.

To understand the difference between x- and γ-ray photoresponse, energy deposition simulation was performed for the GC sample SGL5 and compared with that of the BGO crystal (Fig. 4). In the case of γ rays, a lower energy limit was set for registered events. Due to the smaller density of $\gamma-Ga_2O_3$ NC embedded GCs (3.7 g/cm^3) than that of BGO (7.12 g/cm^3), they exhibit a weaker energy deposition capability. They need a longer penetration depth to fully absorb the incident energy of x rays [cf. Figs. 4(a) and 4(c)], which is also corroborated by the theoretical calculation of x-ray attenuation efficiencies of the samples (Fig. S3 of the Supplemental Material). As shown in Fig. 4(b), the full energy of γ rays can be efficiently absorbed by BGO, whereas only the restricted center part (directly under γ-ray irradiation) of $\gamma-Ga_2O_3$ NC embedded GCs present a certain degree of energy deposition. Owing to the very close densities between PG and GC samples, there is no significant difference in the energy deposition capacity. This indicates that the enhanced XEL of the GCs is indeed caused by the embedded $\gamma-Ga_2O_3$ NCs. However, the weaker scintillation efficiency of the GCs (especially under γ-ray excitation) compared to BGO can be attributed to the less efficient energy absorption and conversion process. Correspondingly, in the γ light excitation light yield test, SGL5 light yield is only about 200 ph/MeV, while BGO is about 8000 ph/MeV (Fig. S4 of the Supplemental Material). The low volume fraction (crystallinity) of $\gamma-Ga_2O_3$ NCs in the GCs may also contribute to the less-than-expected scintillation.

The configuration of a homemade x-ray imaging system is illustrated in Fig. 5(a). An x-ray image of a microchip was obtained using SGL10 as the scintillation material. Chip details can be clearly distinguished in the image. The modulation transfer function (MTF) of the image was determined using the slanted-edge method [40]. The spatial resolution was

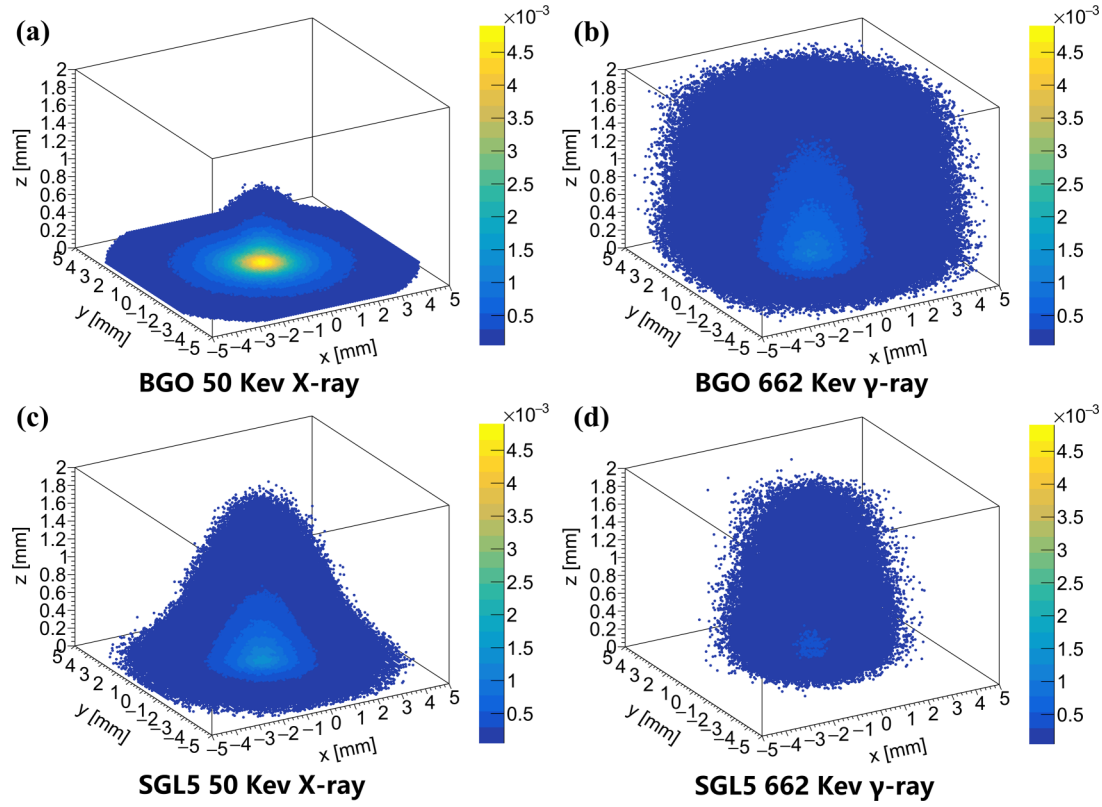

FIG. 4. Monte Carlo simulations of energy deposition in BGO and $\gamma-Ga_2O_3$ NC embedded GCs under x- and γ-ray irradiations.

defined as the spatial frequency at which MTF reaches 0.2 lp/mm, and for SGL10, the image resolution was measured to be 5.1 lp/mm. It is superior to that of the $CsPbBr_3$ perovskite NC embedded GCs (4.1 lp/mm) [62]. To further validate these values, an image was taken of the standard x-ray resolution test mode board [Fig. 7(d)], showing an observation limit ranging 5–6 lp/mm, which is consistent with the calculated MTF value.

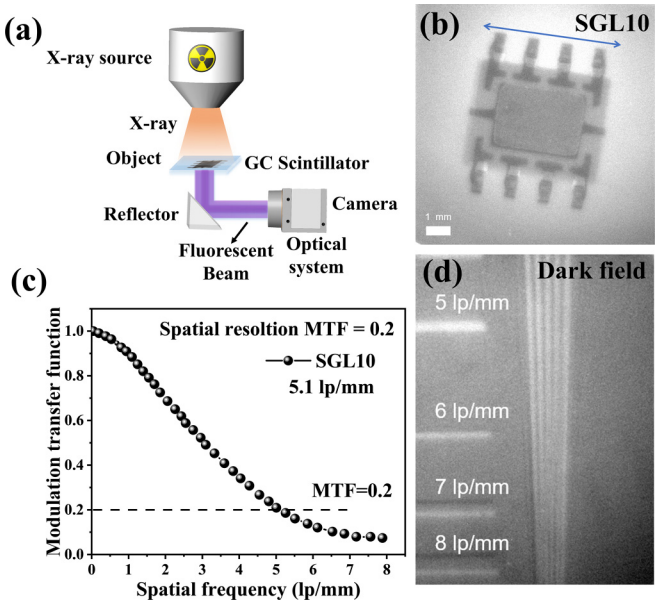

FIG. 5. (a) Schematic of the x-ray imaging system using SGL10 as the scintillator. (b) X-ray image of a microchip. (c) MTF plotted for the x-ray image. The spatial resolution defined when the MTF value reaches 0.2 was determined to be 5.1 lp mm^{-1}. (d) X-ray image of a standard x-ray resolution test pattern plate.

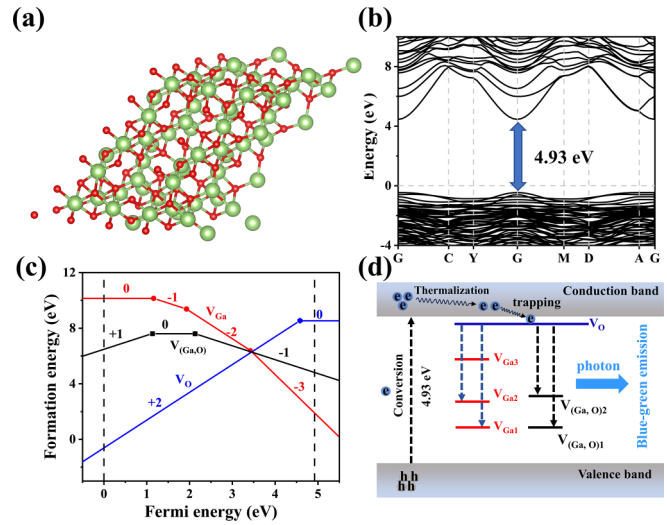

FIG. 6. (a) The unit cell structure of $\gamma-Ga_2O_3$. (b) Band structure of $\gamma-Ga_2O_3$ via the HSE method. (c) The dependence of the DFE values over the corresponding Fermi level via the HSE method. (d) The defect electronic levels equivalent to the filled circles in (c), alongside their relevant charge states. The arrows indicate possible electronic transitions responsible for the observed blue emission. Also shown is the schematic of the scintillation process in $\gamma-Ga_2O_3$.

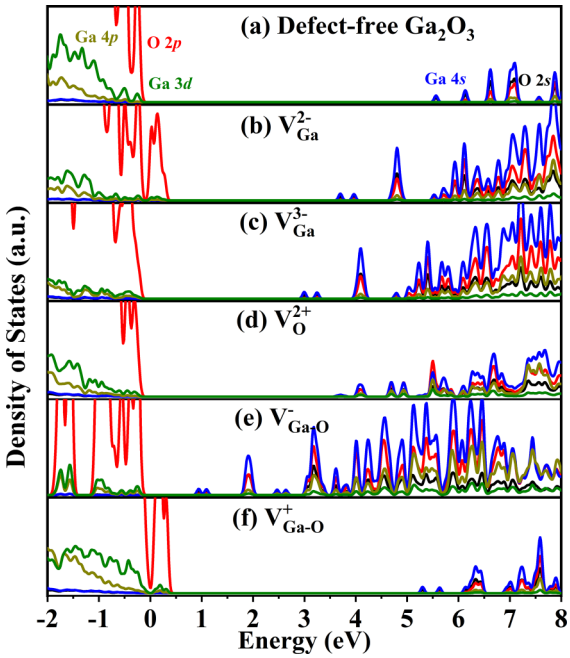

FIG. 7. Partial density of states of (a) defect-free $\gamma-Ga_2O_3$, and $\gamma-Ga_2O_3$ with the charged defects (b)V_{Ga}^{2-}, (c) V_{Ga}^{3-}, (d) V_O^{2+}, (e) $V_{Ga\text{-}O}^{-}$, (f) $V_{Ga\text{-}O}^{+}$.

C. Theoretical calculation of defect-driven luminescence

The defect levels of the $\gamma-Ga_2O_3$ crystal were calculated using the first-principles method. As shown in Fig. 6(a), $\gamma-Ga_2O_3$ demonstrates a cation-deficient cubic spinel structure with the space group $Fd\bar{3}m$, which is analogous to that of $\gamma-Al_2O_3$ [22]. It has been validated that $\gamma-Ga_2O_3$ exhibits a direct band-gap semiconductor structure with a band gap of 4.93 eV. This is in agreement with previous literature [28], as depicted in Fig. 6(b). It is believed that the luminescence of $\gamma-Ga_2O_3$ is primarily driven by the intrinsic defects, and thus understanding the formation and thermodynamic properties of those defects is crucial for elucidating the optical behavior of the material. Figures 6(c) and 6(d) illustrate, respectively, the calculated formation energies and thermodynamic transition levels of various defects. The formation energy of oxygen vacancies (V_O) was found to be negative up to a Fermi energy of 1.92 eV, indicating that V_O spontaneously form below this energy level. The thermodynamic transition level of V_O was determined to be at 4.59 eV, corresponding to a valence shift of +2/0. This suggests that oxygen vacancies act as a donor in the defect-related luminescence of $\gamma-Ga_2O_3$. On the other hand, both gallium vacancies (V_{Ga}) and V_O exhibit positive formation energies within the forbidden band, implying that their generation requires a small amount of external energy. This suggests that the presence of the above two defects can be influenced and controlled by external factors, such as doping or processing conditions [13].

Previously, the blue-green emissions of $\gamma-Ga_2O_3$ have been assumed to arise from the tunnel recombination of an electron from an oxygen vacancy donor with a hole on an acceptor, which can be either a gallium ion vacancy or a pair of charged vacancies. The presence of acceptor sites on the surface of $\gamma-Ga_2O_3$ NCs suggests a role of the oxide matrix in stabilizing these sites during crystallization, which is facilitated by the structural mismatch and the presence of gallium vacancies. Here, the defect formation energies of gallium vacancies (V_{Ga}) and gallium-oxygen divacancies ($V_{(Ga,\,O)}$) were calculated, revealing multiple valence states: 0, +1, +2, and +3 for V_{Ga}, with transition energy level positions at 1.17 eV (0/+1, denoted by V_{Ga1}), 1.94 eV (+1/+2, V_{Ga2}), and 3.43 eV (+2/+3, V_{Ga3}), respectively. Additionally, the transition energy levels for the defect pairs $V_{(Ga,O)}$ were determined to be −1/0 at 1.14 eV ($V_{(Ga,\,O)1}$) and 0/+1 at 2.13 eV ($V_{(Ga,\,O)2}$), respectively. Notably, the calculated transitions from V_O to V_{Ga1} and $V_{(Ga,\,O)2}$ at around 2.6 eV precisely align with the experimentally observed emissions at a wavelength of 465 nm. This further reinforces the significance of V_{Ga} or $V_{(Ga,\,O)}$ in the optical properties of $\gamma-Ga_2O_3$. The high-energy level traps associated with V_O and V_{Ga} or $V_{(Ga,\,O)}$ correlate well with the observed blue-green emissions. However, $V_{(Ga,\,O)}$ exhibits a lower defect formation energy, indicating a potentially higher defect concentration and greater thermodynamic stability. Consequently, in the low Fermi level region, $V_{(Ga,\,O)}$ is more likely to contribute to luminescence. It is also important to acknowledge that the complex chemical environment of oxygen in $\gamma-Ga_2O_3$ poses challenges in fully describing the properties solely based on V_O defects. This complexity suggests the presence of additional defect types or oxygen-related interactions that contribute to the overall optical behavior of the material.

Incorporating the density of states (DOS) analysis is instrumental in providing a more profound comprehension of the electron transition dynamics associated with DAP-related defects. In Fig. 7, the valence band maximum (VBM) is primarily attributed to the contributions of 2*p* orbitals from O and 3*d* and 4*p* orbitals from Ga. The conduction band minimum (CBM) is predominantly shaped by the 2*s* orbitals of O and 4*s* orbitals of Ga. To provide a more comprehensive understanding of these electronic characteristics, we conducted an in-depth study on the DOS of defects with lower defect formation energy in Ga_2O_3 in Figs. 7(b)–7(f).

As depicted in Fig. 7(b), the introduction of a Ga vacancy with −2 charged state, denoted as V_{Ga}^{2-}, disrupts the structural symmetry and introduces two unpaired electrons, resulting in a substantial number of defect levels within the band gap. The defect level arising from the hybridization of 2*p* orbitals of O and 3*d* and 4*p* orbitals of Ga resides between 0 and 0.39 eV above the Fermi level. In contrast, the hybridization of 2*s* orbitals of O and 4*s* orbitals of Ga occurs between 3.58 and 3.80 eV, near the bottom of the conduction band. However, no defect states resembling those in the DOS of V_{Ga}^{2-} are observed at the top of the valence band in V_{Ga}^{3-} [in Fig. 7(c)]. Due to the increased number of unpaired electrons in the structure, hybridization between the 2*s* orbitals of O and the 4*s* orbitals of Ga leads to the formation of a more diverse array of defect states, consequently reducing the band gap.

The presence of the vacancy pair $V_{Ga\text{-}O}^{-}$ leads to further reduction in structural symmetry, resulting in a significant decrease in the band gap value in Fig. 7(e). Notably, the influence of a $V_{Ga\text{-}O}^{-}$ on the band gap is significantly greater than that of a reduced number of unpaired electrons in the negatively valent $\gamma-Ga_2O_3$ defect (V_{Ga}) structure. However,

turning to the vacancy pair with positive valence in $\gamma-Ga_2O_3$, Fig. 7(f) showcases the electronic structure exhibiting similarities to that of V_{Ga}^{2-}, with $2p$ orbitals of O and the hybridization of $3d$ and $4p$ orbitals of Ga appearing at the Fermi level. Additionally, the band-gap value of the defect V_O^{2+} is significantly lower than that of the $V_{Ga\text{-}O}^{+}$. In summary, the calculated formation energies and thermodynamic transition levels of various defects shed light on the role of V_O, V_{Ga}, and $V_{(Ga,\,O)}$ pairs in the optical processes of the material. Besides, these diverse defect structures give rise to new trap levels near the VBM or CBM and shallow defects that influence energy transfer processes and excitation transitions. As a result, they significantly impact the occurrence of specific luminescence wavelengths within the sample.

IV. CONCLUSION

The $\gamma-Ga_2O_3$ NCs are grown in the glass matrix by subjecting the precursor glass with the composition of $25SiO_2-45GeO_2-20Ga_2O_3-2.5Na_2O-7.5Li_2O$ (in mol %) to controlled thermal treatment. Due to the small particle size and being free of aggregation of the NCs in the glass matrix, the optical transparency of the GCs is maintained, which is important for various optical applications. Bright XEL emissions in the visible blue-green region are observed from the $\gamma-Ga_2O_3$ NC embedded GCs. The greatest integral XEL intensity of the GCs reaches 50% of that of BGO. A good linear relationship is found between the XEL intensity and the irradiation dose rate, pointing to the potential of the GCs for use in dosimetry. The positive luminescence hysteresis, present in both PL and XEL, can be effectively eliminated by the prolonged UV preirradiation by filling the nonluminous defects. The Monte Carlo simulations ascertain that the large discrepancies in the photoresponse of x and γ rays are related to the energy deposition capability of the GCs. The first-principles calculations provide a comprehensive understanding of the defect-driven luminescence, and attest to the fact that both gallium vacancies and Ga-O divacancies may be involved in the observed DAP recombination. Owing to the lower defect formation energy and greater thermodynamic stability, the Ga-O divacancies are more likely to contribute to the emissions. Using the studied GCs as the scintillation material, an x-ray imaging system is constructed which, in terms of spatial resolution, exhibits performance superior to that of the $CsPbBr_3$ perovskite NC embedded GCs.

ACKNOWLEDGMENTS

We acknowledge the financial support from the National Natural Science Foundation of China (Grants No. 52201008 and No. 52372003), Natural Science Foundation of Heilongjiang Province of China (Grant No. ZD2023E004), Fundamental Research Funds for the Central Universities (Grants No. 3072020CF2515 and No. 3072022CFJ2504), and GHfund B (Grant No. 202302024584), and the State Key Laboratory of Particle Detection and Electronics (Grant No. SKLPDE-KF-202311). Density functional simulations were performed at the Hefei Advanced Computing Center.

All authors contributed to data analysis, discussions, and manuscript preparation.

There are no conflicts of interest to declare.

[1] C. Dujardin, E. Auffray, E. Bourret-Courchesne, P. Dorenbos, P. Lecoq, M. Nikl, A. N. Vasil'ev, A. Yoshikawa, and R.-Y. Zhu, Needs, trends, and advances in inorganic scintillators, IEEE Trans. Nucl. Sci. **65**, 1977 (2018).

[2] M. L. Zaffalon, F. Cova, M. Liu, A. Cemmi, I. Di Sarcina, F. Rossi, F. Carulli, A. Erroi, C. Rodà, J. Perego, A. Comotti, M. Fasoli, F. Meinardi, L. Li, A. Vedda, and S. Brovelli, Extreme γ-ray radiation hardness and high scintillation yield in perovskite nanocrystals, Nat. Photon. **16**, 860 (2022).

[3] M. Nikl and A. Yoshikawa, Recent R&D trends in inorganic single-crystal scintillator materials for radiation detection, Adv. Opt. Mater. **3**, 463 (2015).

[4] T. Yanagida, Inorganic scintillating materials and scintillation detectors, Proc. Jpn. Acad. Ser. B **94**, 75 (2018).

[5] W. Drozdowski, M. Makowski, A. Bachiri, M. E. Witkowski, A. J. Wojtowicz, L. Swiderski, K. Irmscher, R. Schewski, and Z. Galazka, Heading for brighter and faster $\beta-Ga_2O_3$ scintillator crystals, Opt. Mater. X **15**, 100157 (2022).

[6] S. E. Derenzo, M. J. Weber, and M. K. Klintenberg, Temperature dependence of the fast, near-band-edge scintillation from CuI, HgI_2, PbI_2, ZnO:Ga and CdS:In, Nucl. Instrum. Methods Phys. Res. Sect. A **486**, 214 (2002).

[7] Z. Fang, H. Tang, Z. Yang, H. Zhang, Q. Peng, X. Yu, D. Zhou, J. Qiu, and X. Xu, Transparent medium embedded with CdS quantum dots for x-ray imaging, Adv. Opt. Mater. **9**, 2101607 (2021).

[8] N. N. Asemi, M. J. Aljaafreh, S. Prasad, S. Aldawood, and M. S. AlSalhi, Development of a gamma-ray scintillation detector based on blue-emitting oligomers and ZnO nanoparticles, J. King Saud Univ., Sci. **34**, 101967 (2022).

[9] E. D. Bourret-Courchesne, S. E. Derenzo, and M. J. Weber, Development of ZnO:ga as an ultra-fast scintillator, Nucl. Instrum. Methods Phys. Res. Sect. A **601**, 358 (2009).

[10] W. Drozdowski, M. Makowski, M. E. Witkowski, A. J. Wojtowicz, R. Schewski, K. Irmscher, and Z. Galazka, Semiconductor scintillator development: pure and doped $\beta-Ga_2O_3$, Opt. Mater. **105**, 109856 (2020).

[11] A. K. Mondal, L. K. Ping, M. A. Shazni Mohammad Haniff, M. A. Mohd Sarjidan, B. T. Goh, and M. A. Mohamed, Temperature dependence of ultrathin mixed-phase Ga_2O_3 films grown on the $\alpha-Al_2O_3$ substrate via Mist-CVD, ACS Omega **7**, 2252 (2022).

[12] C. Wu, F. Wu, H. Hu, S. Wang, A. Liu, and D. Guo, Review of self-powered solar-blind photodetectors based on Ga_2O_3, Mater. Today Phys. **28**, 100883 (2022).

[13] K. Nguyen and P. V. Radovanovic, Defects and impurities in colloidal Ga_2O_3 nanocrystals: new opportunities for photonics and lighting, Can. J. Chem. **100**, 1 (2022).

[14] J.-X. Chen, S.-T. Hao, Z.-X. Sun, P. Zheng, and J. Tang, Development of the ZnO:Ga nanorod arrays as an alpha particle scintillation screen for the associated particle neutron generator, Appl. Phys. Lett. **120**, 193502 (2022).

[15] C. Venkata Prasad, M. Labed, M. T. Alam Shamim Shaikh, J. Y. Min, T. H. Vu Nguyen, W. Song, K. J. Kim, and Y. S. Rim, Ga_2O_3 − based x-ray detector and scintillators: A review, Mater. Today Phys. **35**, 101095 (2023).

[16] D. Guo, Q. Guo, Z. Chen, Z. Wu, P. Li, and W. Tang, Review of Ga_2O_3 − based optoelectronic devices, Mater. Today Phys. **11**, 100157 (2019).

[17] D. Guo, X. Qin, M. Lv, H. Shi, Y. Su, G. Yao, S. Wang, C. Li, P. Li, and W. Tang, Decrease of oxygen vacancy by Zn-Doped for improving solar-blind photoelectric performance in $\beta-Ga_2O_3$ Thin films, Electron. Mater. Lett. **13**, 483 (2017).

[18] Y. Su, D. Guo, J. Ye, H. Zhao, Z. Wang, S. Wang, P. Li, and W. Tang, Deep level acceptors of Zn-Mg divalent ions dopants in $\beta-Ga_2O_3$ for the difficulty to p-type conductivity, J. Alloys Compd. **782**, 299 (2019).

[19] X. Zhao, W. Cui, Z. Wu, D. Guo, P. Li, Y. An, L. Li, and W. Tang, Growth and characterization of Sn doped $\beta-Ga_2O_3$ Thin films and enhanced performance in a solar-blind photodetector, J. Electron. Mater. **46**, 2366 (2017).

[20] T. Yanagida, G. Okada, T. Kato, D. Nakauchi, and S. Yanagida, Fast and high light yield scintillation in the Ga_2O_3 semiconductor material, Appl. Phys. Express **9**, 042601 (2016).

[21] J. Chen H. Tang, B. Liu, Z. Zhu, M. Gu, Q. Xu, J. Xu, L. Zhou, L. Chen, and X. Ouyang, High-performance x-ray detector based on single-crystal $\beta-Ga_2O_3$:Mg, ACS Appl. Mater. Interfaces **13**, 2879 (2021).

[22] C.-C. Huang and C.-S. Yeh, GaOOH, and β- and $\gamma-Ga_2O_3$ nanowires: preparation and photoluminescence, New J. Chem. **34**, 103 (2010).

[23] N. He, H. Tang, B. Liu, Z. Zhu, Q. Li, C. Guo, M. Gu, J. Xu, J. Liu, M. Xu, L. Chen, and X. Ouyang, Ultra-fast scintillation properties of $\beta-Ga_2O_3$ single crystals grown by floating zone method, Nucl. Instrum. Methods Phys. Res. Sect. A. **888**, 9 (2018).

[24] Y. Takano, Y. Hayashi, J. Fukushima, and H. Takizawa, Room-temperature synthesis of $\gamma-Ga_2O_3$ nanoparticles from gallium metal via ultrasound irradiation, Adv. Powder Technol. **32**, 860 (2021).

[25] M. García-Carrión, J. Ramírez-Castellanos, E. Nogales, and B. Méndez, Temperature-dependent and time-resolved luminescence characterization of $\gamma-Ga_2O_3$ nanoparticles, Nanomaterials **13**, 1445 (2023).

[26] Q. Lu, L. Xu, K. Han, Z. Huang, and P. Yin, Effect of surface modification on the photoluminescent properties of $\gamma-Ga_2O_3$ nanocrystals, Mater. Lett. **344**, 134437 (2023).

[27] M. Biswas and H. Nishinaka, Thermodynamically metastable α -, ε- (or κ-), and $\gamma-Ga_2O_3$: from material growth to device applications, APL Mater. **10**, 060701 (2022).

[28] Y. Teng, L. X. Song, A. Ponchel, Z. K. Yang, and J. Xia, Self-assembled metastable $\gamma-Ga_2O_3$ Nanoflowers with hexagonal nanopetals for solar-blind photodetection, Adv. Mater. **26**, 6238 (2014).

[29] V. N. Sigaev, N. V. Golubev, E. S. Ignat'eva, A. Paleari, and R. Lorenzi, Light-emitting Ga-Oxide nanocrystals in glass: a new paradigm for low-cost and robust UV-to-Visible solar-blind converters and UV emitters, Nanoscale **6**, 1763 (2014).

[30] R. Lorenzi, N. V. Golubev, E. S. Ignat'eva, V. N. Sigaev, C. Ferrara, M. Acciarri, G. M. Vanacore, and A. Paleari, Defect-assisted photocatalytic activity of glass-embedded gallium oxide nanocrystals, J. Colloid Interface Sci. **608**, 2830 (2022).

[31] Z. Gao, L. Niu, F. Zhang, S. Wang, J. Xiao, J. Chen, L. Zhang, J. Ren, and K. Tanaka, Plasmonic metal enhanced broadband near-infrared emission from a transparent nano-glass composite containing hybrid Ag–Metal/$\gamma-Ga_2O_3$: Ni^{2+} nanocrystals, J. Mater. Chem. C **9**, 15918 (2021).

[32] Z. Gao, L. Niu, F. Zhang, S. Wang, J. Xiao, J. Chen, L. Zhang, J. Ren, and K. Tanaka, Controlling selective doping and energy transfer between transition metal and rare earth ions in nanostructured glassy solids, Adv. Opt. Mater. **6**, 1701407 (2018).

[33] S. Lv, J. Tang, J. Chen, P. Liu, J. Guo, Y. Ma, J. Qiu, and S. Zhou, Full-inorganic micro-fiber probe for real-time radiation monitoring, Adv. Mater. Technol. **6**, 2000696 (2021).

[34] B. Sun, Y. Xie, Y. Zhao, X. Li, J. Chen, Y. Song, L. Zhao, Z. Li, H. Zhao, J. Ren, and J. Zhang, A highly robust Ce^{3+} − doped and Gd^{3+} − mixed $KLaF_4$ nano-glass composite scintillator, J. Mater. Chem. C **9**, 17504 (2021).

[35] L. Niu, S. Wang, Z. Sui, Y. Song, L. Zhao, L. Liu, J. Ren, and J. Zhang, Highly stable $CsPbBr_3$ perovskite quantum dot-doped tellurite glass nanocomposite scintillator, Opt. Lett. **46**, 3448 (2021).

[36] L. E. Ratcliff, T. Oshima, F. Nippert, B. M. Janzen, E. Kluth, R. Goldhahn, M. Feneberg, P. Mazzolini, O. Bierwagen, C. Wouters *et al.*, Tackling disorder in $\gamma-Ga_2O_3$, Adv. Mater. **34**, 2204217 (2022).

[37] H. Y. Playford, A. C. Hannon, E. R. Barney, and R. I. Walton, Structures of uncharacterised polymorphs of gallium oxide from total neutron diffraction, Chem. Eur. J. **19**, 2803 (2013).

[38] M. Zinkevich, F. M. Morales, H. Nitsche, M. Ahrens, M. Rühle, and F. Aldinger, Microstructural and thermodynamic study of $\gamma-Ga_2O_3$, Int. J. Mater. Res. **95**, 756 (2004).

[39] M. Hegde, T. Wang, Z. L. Miskovic, and P. V. Radovanovic, Origin of size-dependent photoluminescence decay dynamics in colloidal $\gamma-Ga_2O_3$ nanocrystals, Appl. Phys. Lett. **100**, 141903 (2012).

[40] W. Li, Z. Sui, C. Fan, C. Wang, Y. Zhu, J. Ren, and J. Zhang, Intense radioluminescence from transparent $CsGd_2F_7$: Ce^{3+} nano-glass scintillator, J. Eur. Ceram. Soc. **43**, 6331 (2023).

[41] J. Allison, K. Amako, J. Apostolakis, H. Araujo, P. Arce Dubois, M. Asai, G. Barrand, R. Capra, S. Chauvie, R. Chytracek *et al.*, Geant4 developments and applications, IEEE Trans. Nucl. Sci. **53**, 270 (2006).

[42] G. Kresse and D. Joubert, From ultrasoft pseudopotentials to the projector augmented-wave method, Phys. Rev. B **59**, 1758 (1999).

[43] G. Kresse and J. Furthmüller, Efficiency of ab-initio total energy calculations for metals and semiconductors using a plane-wave basis set, Comput. Mater. Sci. **6**, 15 (1996).

[44] G. Kresse and J. Furthmüller, Efficient iterative schemes for ab initio total-energy calculations using a plane-wave basis set, Phys. Rev. B **54**, 11169 (1996).

[45] J. P. Perdew, K. Burke, and M. Ernzerhof, Generalized gradient approximation made simple, Phys. Rev. Lett. **77**, 3865 (1996).

[46] J. Heyd, G. E. Scuseria, and M. Ernzerhof, Hybrid functionals based on a screened coulomb potential, J. Chem. Phys. **118**, 8207 (2003).

[47] A. V. Krukau, O. A. Vydrov, A. F. Izmaylov, and G. E. Scuseria, Influence of the exchange screening parameter on the

performance of screened hybrid functionals, J. Chem. Phys. **125**, 224106 (2006).

[48] P. Deák, Q. Duy Ho, F. Seemann, B. Aradi, M. Lorke, and T. Frauenheim, Choosing the correct hybrid for defect calculations: a case study on intrinsic carrier trapping in $\beta-Ga_2O_3$, Phys. Rev. B **95**, 075208 (2017).

[49] H. J. Monkhorst and J. D. Pack, Special points for brillouin-zone integrations, Phys. Rev. B **13**, 5188 (1976).

[50] S. Yoshioka, H. Hayashi, A. Kuwabara, F. Oba, K. Matsunaga, and I. Tanaka, Structures and energetics of Ga_2O_3 polymorphs, J. Phys.: Condens. Matter **19**, 346211 (2007).

[51] See Supplemental Material at http://link.aps.org/supplemental/10.1103/PhysRevB.108.155414 for the theoretical calculation of formation energy; positive PL Hysteresis Characteristics of the Samples; X-ray attenuation properties and imaging capability; gamma radiation response.

[52] S. Lany and A. Zunger, Assessment of correction methods for the band-gap problem and for finite-size effects in supercell defect calculations: case studies for ZnO and GaAs, Phys. Rev. B **78**, 235104 (2008).

[53] S.-H. Wei and S. B. Zhang, Chemical trends of defect formation and doping limit in II-VI semiconductors: the case of CdTe, Phys. Rev. B **66**, 155211 (2002).

[54] G. Tang, Z. Hua, S. Qian, X. Sun, H. Ban, H. Cai, S. Li, H. Liu, S. Liu, L. Ma, L. Qin, X. Sun, Z. Wang, Y. Wen, Q. Wu, Y. Zhu, and L. Zhang, Optical and scintillation properties of aluminoborosilicate glass, Opt. Mater. **130**, 112585 (2022).

[55] P. Meejitpaisan, R. Doddoji, S. Kothan, and J. Kaewkhao, Photo and X-Ray Luminescence Characteristics of $CeF^{3+} - DopedSiO^{2+}$ $B_2O_3 + AlF_3 + NaF + CaF_2$ scintillating glasses, Radiat. Meas. **158**, 106853 (2022).

[56] V. B. Sreedhar, R. Doddoji, K. K. Kumar, and V. R. Minnam Reddy, A Study of NIR emission and associated spectroscopic properties of $Nd^{3+} : P_2O_5 + K_2O + Al_2O_3 + ZnF_2$ glasses for 1.06 Mm laser applications, J. Non-Cryst. Solids **553**, 120521 (2021).

[57] T. Wang, S. S. Farvid, M. Abulikemu, and P. V. Radovanovic, Size-tunable phosphorescence in colloidal metastable $\gamma-Ga_2O_3$ nanocrystals, J. Am. Chem. Soc. **132**, 9250 (2010).

[58] L. Binet and D. Gourier, Origin of the blue luminescence of $\beta-Ga_2O_3$, J. Phys. Chem. Solids **59**, 1241 (1998).

[59] G. P. Pazzi, P. Fabeni, C. Susini, M. Nikl, E. Mihokova, N. Solovieva, K. Nitsch, M. Martini, A. Vedda, S. Baccaro, A. Cecilia, and V. Babin, Defect states induced by UV–Laser irradiation in scintillating glasses, Nucl. Instrum. Methods Phys. Res. Sect. B **191**, 366 (2002).

[60] I. Veronese, C. De Mattia, M. Fasoli, N. Chiodini, M. C. Cantone, F. Moretti, C. Dujardin, and A. Vedda, Role of optical fiber drawing in radioluminescence hysteresis of Yb-doped silica, J. Phys. Chem. C **119**, 15572 (2015).

[61] F. Moretti, G. Patton, A. Belsky, A. G. Petrosyan, and C. Dujardin, Deep traps can reduce memory effects of shallower ones in scintillators, Phys. Chem. Chem. Phys. **18**, 1178 (2016).

[62] W. Ma, T. Jiang, Z. Yang, H. Zhang, Y. Su, Z. Chen, X. Chen, Y. Ma, W. Zhu, X. Yu, H. Zhu, J. Qiu, X. Liu, X. Xu, and Y. Yang, Highly resolved and robust dynamic x-ray imaging using perovskite glass-ceramic scintillator with reduced light scattering, Adv. Sci. **8**, 2003728 (2021).